The Astronomical Journal, 172:268 (15pp), 2026 November https://doi.org/10.3847/1538-3881/aeaa57
© 2026. The Author(s). Published by the American Astronomical Society.
OPEN ACCESS

Precise Physical and Kinematical Parameters of Massive Eclipsing Binaries in the Small Magellanic Cloud

M. Kaya[1], Ö. Çakirli[1], B. Hoyman[1], O. Özdarcan[1], T. Yontan[2], and R. Canbay[3]
[1] Ege University, Science Faculty, Astronomy and Space Science Department, 35100, Bornova, Izmir, Türkiye; omur.cakirli@ege.edu.tr
[2] Istanbul University, Faculty of Science, Department of Astronomy and Space Sciences, 34119, Beyazit, Istanbul, Türkiye
[3] Akdeniz University, Faculty of Science, Department of Space Sciences and Technologies, 07058, Antalya, Türkiye
Received 2026 May 15; revised 2026 August 6; accepted 2026 September 4; published 2026 October 15

Abstract

The formation of massive stars serves as an important field of study, requiring research into whether these stars need to form together within clusters of low-mass stars or whether they are able to form independently. Recently, there has been an increase in the number of massive stars found far from clusters in the Milky Way and Small Magellanic Cloud (SMC). The existence of isolation and composition in binary systems is an uncommon phenomenon among massive stars, and their rare occurrence presents valuable insights that are regarded as evidence in this field. This research looks for ways to increase the catalog of identified massive stars in eclipsing binaries, particularly those that show significant indications of isolation. As a first step, we are analyzing the eight double-lined spectroscopic binaries in the SMC, as detailed in the OGLE variable star catalogs, with the goal of identifying their astrophysical properties. Then we examine the expected locations and characteristics of binary stars thought to be part of a cluster, using absolute parameters and a cross-validation approach to determine the connection between kinematic analysis and these parameters. If the kinematic connection with the cluster and the physical parameters match precisely with the cluster's isochrone, such stars could act as reliable standard candles for determining the cluster's distance and age.

Unified Astronomy Thesaurus concepts: Small Magellanic Cloud (1468); Eclipsing binary stars (444); Fundamental parameters of stars (555); Binary stars (154); Close binary stars (254); Stellar evolution (1599); Hertzsprung Russell diagram (725); Open star clusters (1160)

Materials only available in the online version of record: machine-readable table

1. Introduction

The prevailing view is that stellar clusters are typically not formed in isolation; rather, they represent the densest collections of larger stellar aggregates and complexes (B. G. Elmegreen 2011) within a hierarchical framework of stellar structures that extends to galactic scales (D. A. Gouliermis et al. 2010; S. Hony et al. 2015). Massive field stars, in contrast, are not found in clusters but rather appear to exist in apparent isolation, whereas cluster stars are formed together in large aggregates simultaneously; field stars have multiple origins.

M. S. Roberts (1957) was the first to investigate whether all massive stars are formed in clusters or whether a considerable number may instead form in isolation as field stars. Furthermore, C. J. Lada & E. A. Lada (2003) and S. F. Portegies Zwart et al. (2010) indicated that stellar formation in clusters demonstrates variability in size, mass, and stellar composition. Such variation ranges from small, compact groups of protostars that remain embedded in their primordial stellar formation regions to large young massive clusters containing approximately $10^4\,M_\odot$ of mass. Some of these massive field stars may only begin to scratch the surface of understanding small groups of physically associated stars, while others appear to be `runaway` stars that have been dynamically ejected from clusters. Studies that are considered to be the most significant on this topic concentrate on the origins of field stars. The research conducted by M. S. Oey & J. B. Lamb (2012) studied the origins of field stars, which account for around 20%–25% of the massive stars that are found in galaxies, and distinguished between in situ formations and runaway forms. While stars that are removed from their clusters due to dynamic interactions or supernova explosions in binary systems are known as runaway stars, M. S. Oey & J. B. Lamb (2012) showed strong evidence that some massive stars can indeed form in situ within small groups or even in isolation. This is in contrast to the traditional viewpoint, which implies that massive stars must form in massive clusters. The study by J. B. Lamb et al. (2016) was particularly important in this regard. A comprehensive spectroscopic investigation of OB-type stars in the Small Magellanic Cloud (SMC) was carried out, focusing on the influence of the stellar formation environment on binarity. In the end, they considered the potential that the ratio of binary stars in isolated formations might be less or exhibit different period distributions in comparison to stars found within a cluster.

Furthermore, H. Sana et al. (2012) provided statistical evidence that the supernova scenario, initially suggested by A. Blaauw (1961), is not just an infrequent occurrence but rather an essential part of the evolution of massive stars. This, along with observations conducted in environments like the SMC or Tarantula Nebula, clearly elucidates how escaped stars rise to the galactic halo and the reasons behind some being classified as isolated fast rotator stars (V. Hénault-Brunet et al. 2012; H. Sana 2013; H. Sana et al. 2013).

While there may be high-mass stars that formed in true isolation, if they exist, such occurrences are likely to be extremely rare. Our study aims to identify massive eclipsing binaries in the SMC and investigate their origin via

Original content from this work may be used under the terms of the Creative Commons Attribution 4.0 licence. Any further distribution of this work must maintain attribution to the author(s) and the title of the work, journal citation and DOI.

Table 1
Basic Information for the OGLE-SMC Eclipsing Binaries in the NGC 290 Cluster Considered in This Work

Target (*OGLE*)	R.A. (J2000)	Decl. (J2000)	*V* (mag)	Orbital Period (days)	Spectral Type
SMC-ECL-2194	00:51:35.8	−73:12:45.3	17.06	1.3029	B[a]
SMC-ECL-2198	00:51:37.2	−73:05:50.7	17.44	1.3298	B[a]
SMC-ECL-2096	00:51:16.8	−73:13:02.3	15.94	1.8089	B[a]
SMC-ECL-2073	00:51:11.4	−73:05:21.7	16.78	1.9394	B1+B1[b]
SMC-ECL-2213	00:51:40.3	−73:13:20.8	15.36	2.3238	B0[c]
SMC-ECL-1947	00:50:40.5	−73:12:56.2	16.12	2.4013	B3 V[a]
SMC-ECL-1903	00:50:30.2	−73:07:38.7	16.91	3.9426	B3 V[a]
SMC-ECL-1105	00:46:50.4	−73:07:30.3	15.84	9.0576	⋯

Notes. The stars are listed in order of increasing orbital period. All targets are massive, early-type stars, as inferred from photometry.
[a] C. L. Watson et al. (2006).
[b] R. W. Hilditch et al. (2005).
[c] J. B. Hutchings & I. B. Thompson (1988).

photometric and spectroscopic observations. We also get the benefit of kinematic analysis of the identified binaries to provide a wider perspective on the problem. Such a study could reveal whether they formed in an isolated environment or in a stellar cluster or association. Our research is structured as follows: Section 2 presents the observational data sources used for modeling our systems. Section 3 presents a comprehensive overview of the methodology used to derive radial velocity (RV) from spectroscopic data. The approach taken to resolve both the RV and light curves of the systems is outlined. Furthermore, it outlines the procedure to determine the atmospheric parameters, analyzing the membership of target stars in the NGC 290 cluster and analyzing their detailed kinematics. Section 4 outlines the carried-out solutions for each system and evaluates their evolutionary stages. Section 5 sets out our conclusions.

2. Observations

2.1. Photometry

In this study, we used OGLE photometry from the OGLE-II (A. Udalski et al. 1997), OGLE-III (A. Udalski 2003), and OGLE-IV (A. Udalski et al. 2015) databases. The data were collected utilizing the 1.3 m Warsaw telescope at Las Campanas Observatory in Chile, operated by the Carnegie Institution for Science. The photometric data collected from OGLE utilize filters comparable to the standard *V* and *I* photometric bands; for instance, the OGLE *I* band, centered at 8000 Å, corresponds precisely with the standard Kron–Cousins *I*-band filter. The OGLE *V* band, centered at 5500 Å, shows minor variations compared to the standard Johnson *V* band (A. Udalski et al. 2015).

We investigated eight binary systems, as previously defined by M. Pawlak et al. (2016) and listed in Table 1, which includes the OGLE IDs of the objects. The OGLE online database[4] provides public access to photometric data. Among the target stars presented in Table 1, only TIC 181042539 (SMC-ECL-2213) had TESS (Transiting Exoplanet Survey Satellite, G. R. Ricker et al. 2015) data available, and they were used for the analysis.

Table 2
Summary of Spectroscopic Observations

Target (OGLE)	Observation Dates	Exposure (s)	SNR	$N_{\rm Giraffe}$
SMC-ECL-2194	2003/11/16–23	2595	35.1	16
SMC-ECL-2198	2003/11/16–25	2595	29.4	16
SMC-ECL-2096	2003/11/16–23	2600	57.9	16
SMC-ECL-2073	2003/11/16–23	2595	66.2	16
SMC-ECL-2213	2003/11/16–23	2700	71.2	16
SMC-ECL-1947	2003/11/16–25	2700	54.7	21
SMC-ECL-1903	2003/11/16–23	2595	40.1	21
SMC-ECL-1105	2003/10/02–25	2700	61.8	5

2.2. Spectroscopy

This research uses the archival ESO spectroscopic database (Science Archive Facility[5]) gathered with the multiobject spectrograph FLAMES, which includes the GIRAFFE spectrograph. The data were obtained via programs 072.D-0577(A), 092.D-0110(A), 072.A-0474(A), 079.D-0562(A), 190.D-0237(A), 094.D-0056(A), 097.D-0150(A), 098.D-0876(A), and 106.21CY.001. FLAMES functions as the multiobject intermediate- and high-resolution spectrograph of the Very Large Telescope (VLT), installed at the UT2 (Kueyen telescope) in Paranal, Chile. The spectra were acquired with the GIRAFFE `LR02` setup along with its corresponding `LR02` setting, which provides a spectral resolving power of $\lambda/\delta\lambda \sim 6500$. This resolving power is adequate to identify stars where helium lines might be influenced by nebular contamination, as established through inspection of `Balmer` lines. The `LR02` data offer continuous wavelength coverage from 3964 to 4567 Å, allowing access to multiple spectral lines that are ideal for precise RV measurements. In this GIRAFFE configuration, observations of eight stars resulted in the collection of a total of 127 spectra. The details of these observations are presented in Table 2.

The essential step in analyzing the obtained spectra is the normalization process. This is evident in studies on stellar abundances (e.g., S. Blanco-Cuaresma et al. 2014; S. G. Sousa et al. 2015; V. Adibekyan et al. 2016) and in the analysis of low-mass stellar atmospheres. The final step is cosmic correction, which is equally important as normalization.

[4] https://ogledb.astrouw.edu.pl/ogle/

[5] http://archive.eso.org/wdb/wdb/adp/phase3_main/form

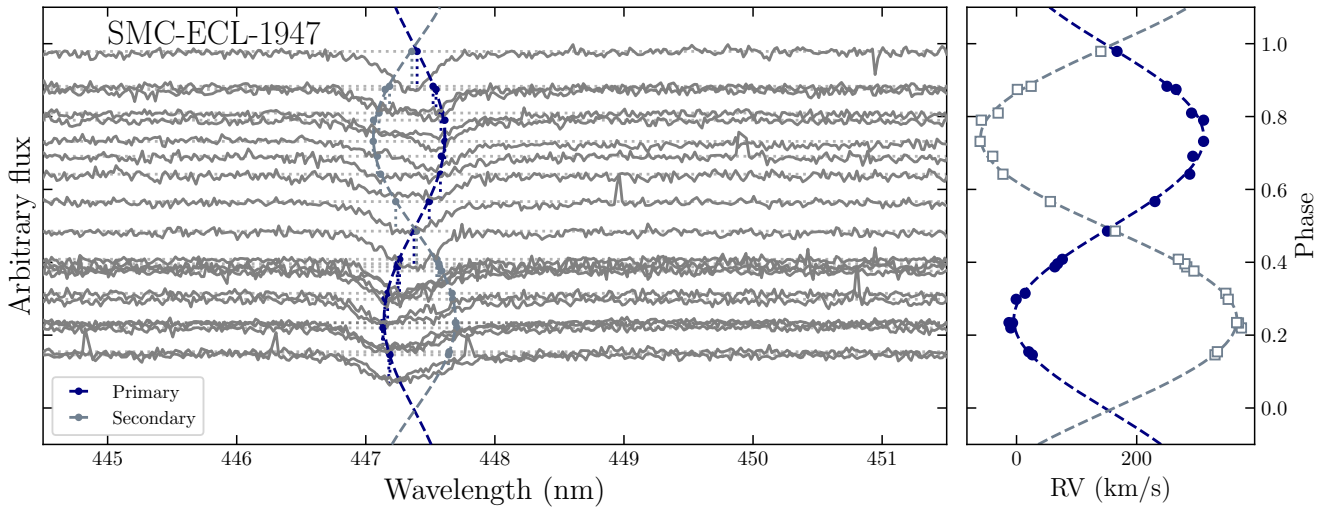

Figure 1. The left panel shows a set of absorption lines involving a secondary component, which matches the orbital period cycle of the system. The variation of the He I λ4471 Å line profiles is represented by dashed lines. The right panel displays the RV of the absorption lines. The filled circles on the RV plot indicate the primary, whereas the open squares represent the secondary.

The RVs for each object were established by using cross correlation of the observed spectra with a synthetic template, constructed by combining synthetic spectra that correspond to both the primary and secondary components. We adopt the cross-correlation function (CCF; J. Tonry & M. Davis 1979) method to detect the RV signals of the components. This method allowed us to detect signals from these components. In practice, we utilize the RAVESPAN code (Radial Velocity and Spectrum Analyser; B. Pilecki et al. 2017) to apply the CCF method. The template spectra used in the CCF method were specifically created for practical measurements of RVs in stars with effective temperatures between 10,000 and 30,000 K, in increments of 3000 K. Table A1 presents the velocity values for both components of our SB2 systems, including their associated errors and the heliocentric Julian dates of the observations. Figure 1 shows the normalized spectra shifted along the orbital phase of OGLE SMC-ECL-1947.

3. Analysis Methods

3.1. Atmospheric Parameters

We used a PYTHON code that makes use of the ISPEC routines of S. Blanco-Cuaresma et al. (2014) and S. Blanco-Cuaresma (2019) to generate model spectra in order to determine the atmospheric parameters of each component star in all eight of our binary systems. Depending on the effective temperature, one of the SPECTRUM ATLAS9.CASTELLI grid, TLUSTY BSTAR2006 grid, or TLUSTY OSTAR2002 grid was used to generate the synthetic spectra.

The code optimizes up to 10 stellar parameters for each component simultaneously. These parameters include surface temperature ($T_{\rm eff\,1,2}$), surface gravity ($\log g_{1,2}$), metallicity ($[M/H]_{1,2}$), alpha enhancement ($[\alpha{\rm Fe}]_{1,2}$), microturbulent velocity ($\nu_{\rm mic,1,2}$), macroturbulent velocity ($\nu_{\rm mac,1,2}$), projected rotational velocity ($v \sin i_{1,2}$), limb darkening coefficients ($\rm LD_{1,2}$), RV ($\rm RV_{1,2}$), and the fractional light contribution of each component to the total light ($l_{\rm frac_{1,2}}$).

The individual spectra of each component were synthesized with the respective parameter set and scaled according to the light contribution, shifted by the RV value. These spectra were then combined to form a composite spectrum that was then compared with the observed spectrum. This is an iterative process to home in on the parameter set to get it right. This synthetic composite spectrum can cover the whole observed spectrum or be limited to certain segments to reduce the computational time and improve the quality of the solutions. For a correct determination of the expected atmospheric parameters, attention should be paid to certain lines in the spectral range of the stars selected for the analysis. We used the wavelength range 400–450 nm, in which the spectral lines of both components are visible.

The solution involves fixing certain parameters, such as $\nu_{\rm mic}$, $\nu_{\rm mac}$, and limb darkening, while establishing relationships for others, including $[M/H]_1 = [M/H]_2$ and $l_{\rm frac_2} = 1 - l_{\rm frac_1}$. This method limits the solution according to these defined links. Furthermore, it is possible to define variance ranges for independent parameters, which enables the solution to be restricted within these specified ranges. The initial parameter-seeking setup utilizes broad ranges and substantial step sizes to guarantee the identification of the global minimum while minimizing computational time. Nonetheless, differentiating between micro- and macroturbulent velocities, as well as rotational velocity, poses a significant challenge. This challenge necessitates spectra with exceptionally high resolution and a strong signal-to-noise ratio (SNR) to effectively tackle the degeneracy among these parameters (A. P. Doyle et al. 2014). To address this degeneracy and create a standard procedure for analyzing spectra with lower resolution and SNR, we adopt $\nu_{\rm mic}$ as $2\,{\rm km\,s^{-1}}$ to align with the grid we are using. Our initial analyses have shown extremely high projected rotational velocities, which could greatly diminish the effect of macroturbulence in spectral lines; therefore, we have set $\nu_{\rm mac}$ to zero.

The EMCEE package (D. Foreman-Mackey et al. 2013), a realistic implementation of the Markov Chain Monte Carlo (MCMC) method, was used to identify the best-fitting parameters and their uncertainties. First, we set the $[M/H]$ parameter as well as the effective temperature and $\log g_{1,2}$ parameters for each component to be configurable. We also included $v \sin i$ parameters as modifiable if we saw rotational broadening in earlier trials. The initial fixed parameters for light-curve modeling were the T_1 and $[M/H]$ parameters that

were determined at the end of the MCMC run. After that, we computed the target system's absolute attributes by modeling light curves. For the next MCMC run, we fixed the $\log g_{1,2}$ values of the components among these attributes. By successfully constraining the $\log g_{1,2}$ values and resolving any degeneracy among the remaining changeable parameters, this approach produces atmospheric parameter estimates that are more accurate. Graphical representations of the results of the MCMC analysis and the consistency between the observed and fitted model spectra for the systems are presented in Figure 2. Table 3 contains a tabulation of the numerical results. The reported uncertainties, particularly for the effective temperatures, seem too low (less than 130 K) for several systems given the resolution and SNR of the measured spectra as well as the spectroscopic characteristics of the target systems. The real uncertainties, which are mostly caused by ambiguity in the continuum level, are expected to be approximately 150 K.

3.2. Light and RV Curve Modeling

The light and measured RV curves were simultaneously modeled using the Wilson–Devinney (hereafter WD) software (R. E. Wilson & E. J. Devinney 1971; R. E. Wilson 1979). To utilize the WD code efficiently and rapidly, we employ the PYWD 2015 framework. This framework provides a graphical user interface for the 2015 version of the code and facilitates the simultaneous analysis of light and RV curves (R. E. Wilson & W. Van Hamme 2014; O. Güzel & O. Özdarcan 2020). The primary advantage of the code is that the WD program uses a differential correction algorithm to determine a set of parameters that characterize observables in the solution, while one of the modeling options, `Mode 2`, is intended for detached eclipsing binaries. Another aspect to consider is `Mode 5` of the WD code, which is used for analyzing the light curves of semidetached eclipsing binary stars, where the secondary star fills its limiting Roche lobe, and differs from `Mode 2`. While we employed the albedo (A) and gravity brightening (g) coefficients for both components, these were set to 1.0, which are standard values for stars with radiative envelopes (J. B. Rafert & L. W. Twigg 1980). In our modeling, we utilized the linear limb darkening law, incorporating automatically updated coefficients from precomputed tables provided by W. van Hamme (1993), along with the stellar atmosphere formulation.

The initial values for the orbital parameters have been estimated based on a preliminary geometrical analysis of the RV curve. One of the most important initial parameters of the analysis is the temperature of the primary component (T_1), which we maintained as a constant throughout the light and RV solution. We established the temperature of the primary star by making the assumption that this component is the hotter one, and we fixed the value of T_1 by using the data from the atmospheric analysis that we had previously obtained. In the same way, we made the assumption that the metallicity was consistent with the value that was calculated based on the analysis of the atmosphere. We initiated the solution process by simultaneously modifying the following parameters: eccentricity (e), semimajor axis (a), orbital inclination (i), longitude of the periastron (ω), dimensionless surface

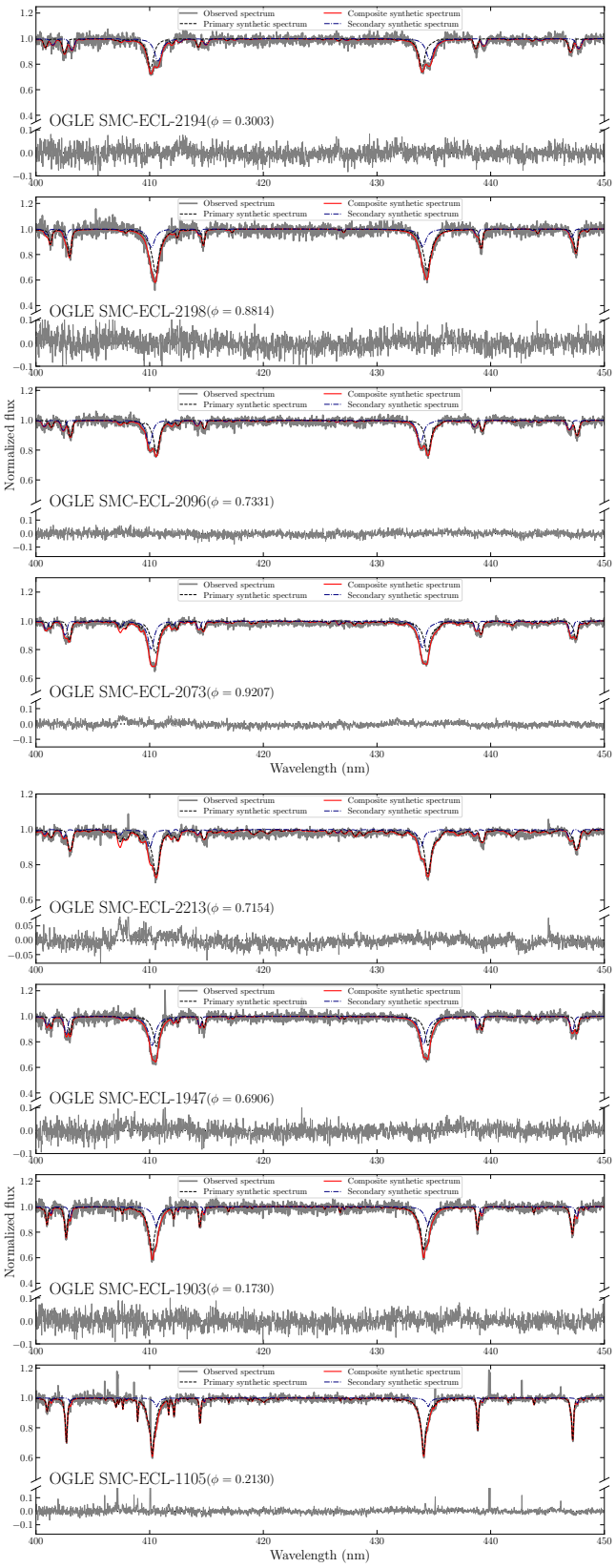

Figure 2. The composite spectra of the systems are compared to a combined synthetic model, which is represented by the dashed line for the primary and the dotted–dashed line for the secondary star. This model is created from the models that match each system the best.

Table 3
Atmospheric Analysis Results of the Target Systems

Catalog IDs	$T_{\rm eff}$ (K)	$\log g$[a] (dex)	$[M/H]$ (dex)	$v \sin i_{\rm obs}$ (km s^{-1})	Reduced χ^2
SMC-ECL-2194	$29{,}050^{+30}_{-50}$	4.31	$-1.198^{+0.022}_{-0.033}$	213^{+7}_{-11}	1.6021
	$26{,}450^{+20}_{-70}$	4.32		177^{+6}_{-15}	
SMC-ECL-2198	$26{,}300^{+17}_{-33}$	3.97	$-1.009^{+0.013}_{-0.031}$	172^{+3}_{-9}	2.0129
	$19{,}290^{+40}_{-52}$	4.10		125^{+4}_{-9}	
SMC-ECL-2096	$31{,}250^{+23}_{-83}$	3.80	$-1.004^{+0.009}_{-0.012}$	174^{+8}_{-17}	2.0011
	$20{,}400^{+19}_{-93}$	3.66		191^{+6}_{-13}	
SMC-ECL-2073	$30{,}000^{+32}_{-103}$	3.77	$-0.267^{+0.009}_{-0.013}$	144^{+5}_{-9}	2.1102
	$20{,}100^{+41}_{-121}$	3.48		165(13)	
SMC-ECL-2213	$28{,}510^{+26}_{-91}$	3.70	$0.089^{+0.041}_{-0.044}$	212^{+4}_{-8}	1.1255
	$18{,}210^{+44}_{-101}$	3.71		179^{+7}_{-11}	
SMC-ECL-1947	$12{,}280^{+22}_{-38}$	3.81	$-0.489^{+0.032}_{-0.033}$	117^{+7}_{-17}	2.0033
	9520^{+39}_{-77}	4.32		79^{+5}_{-11}	
SMC-ECL-1903	$19{,}400^{+24}_{-67}$	3.98	$0.193^{+0.022}_{-0.031}$	81^{+3}_{-9}	2.0012
	$17{,}800^{+61}_{-111}$	4.02		75^{+6}_{-13}	
SMC-ECL-1105	$32{,}300^{+24}_{-87}$	3.90	$-0.877^{+0.019}_{-0.025}$	52^{+2}_{-9}	1.9441
	$20{,}725^{+71}_{-122}$	3.89		58^{+3}_{-10}	

Notes. We adopted the same metallicity for both components.
[a] The parameter is obtained from the light-curve solution and fixed during the atmospheric analysis.

potentials (Ω_1, Ω_2), systemic velocity (V_γ), mass ratio ($q = M_2/M_1$), effective temperature of the secondary component (T_2), orbital period (P), phase shift (φ), luminosity of the primary component in the specified filter (L_1), and third light (ℓ_3). After reaching a satisfactory solution, we present the best-fitting light curves and RV curves derived from the binary model, along with their corresponding $O-C$ residuals, in Figure 3. The results of the best-fitting models are summarized in Tables 4 and 5, which indicates that the convergence solutions, along with the associated parameter errors provided by the WD code, are underestimated. In order to overcome this limitation, we will compute the parameter errors, as detailed in the Subsection 3.3.

3.3. Absolute Dimensions and Distance

Prior to comparing the model predictions with observational data, we took extreme care in determining the orbital and stellar parameters of the systems. The physical parameters are obtained from models of light and RV curves, using a FORTRAN-based code called JKTABSDIM, developed by J. Southworth et al. (2005). An approach known as perturbation analysis was used to derive the output error bars. The code requires data derived from modeling solutions, which include the period, RV semiamplitude, inclination, eccentricity, component temperatures, fractional radii, reddening, and availability of photometry with the visual magnitudes of the system in the Johnson–Cousins *UBVRI* and the Two Micron All-Sky Survey (2MASS) JHK_s bands. Based on the provided information, the code computes the radius, mass, and luminosity for each component. For calculating luminosity, the bolometric correction data sourced from L. Girardi et al. (2002) are utilized.

Measuring the distance of the systems is crucial for our understanding of their formation and evolution. In this context, it has been recently proposed that stellar clustering might be the key to shaping the structural architecture of galaxies. Assessing interstellar extinction is essential for numerous fields of astronomical research. Nonetheless, reddening continues to be a primary impediment to the precise measurement of interstellar distances. The interstellar extinction for each of our target stars was determined using two methods, as outlined by Ö. Çakırlı et al. (2023), which provides a detailed explanation comparable to this study. Additionally, the distances to the systems can be readily quantified.

There are two methods for estimating reddening values within the context of the Magellanic Clouds. The first method uses the reddening maps established by R. Haschke et al. (2011). Incorporating recent maps would minimally affect findings, with adjustments of less than −0.003 mag for D. M. Skowron et al. (2021) and a potential increase of +0.008 mag for M. Górski et al. (2020). The second method encompasses effective temperatures from the atmospheric analyses discussed in Section 3.1. Effective temperatures were employed to derive intrinsic $(V-I)$ and $(V-K)$ colors through relevant calibrations (G. P. di Benedetto 1998; M. L. Houdashelt et al. 2000; I. Ramírez & J. Meléndez 2005). These intrinsic colors were compared to observed colors from an initial solution to calculate $E(V-I)$ and $E(V-K)$ color excesses, subsequently leading to an estimated $E(B-V)$. The average reddening was computed based on components with estimates from both methods. The results, including averaged reddening values and final distances, are detailed in Tables 4 and 5, which also showcase physical properties, distances, and associated uncertainties.

It seems that the predicted distances of the systems are in agreement with the average distance of the NGC 290 cluster. Based on E. Chiosi & A. Vallenari (2007), the distance to the NGC 290 cluster was confirmed to be 60.3 kpc. On the other hand, D. Graczyk et al. (2020) found the distance to the SMC to be 62.4 kpc, reaching an accuracy of 2%, which is dependent on late-type eclipsing binary stars. All of the distances that we found for the target stars are in agreement with the ones that were published in the research. Kinematic analysis allows for the verification of the positions of the stars

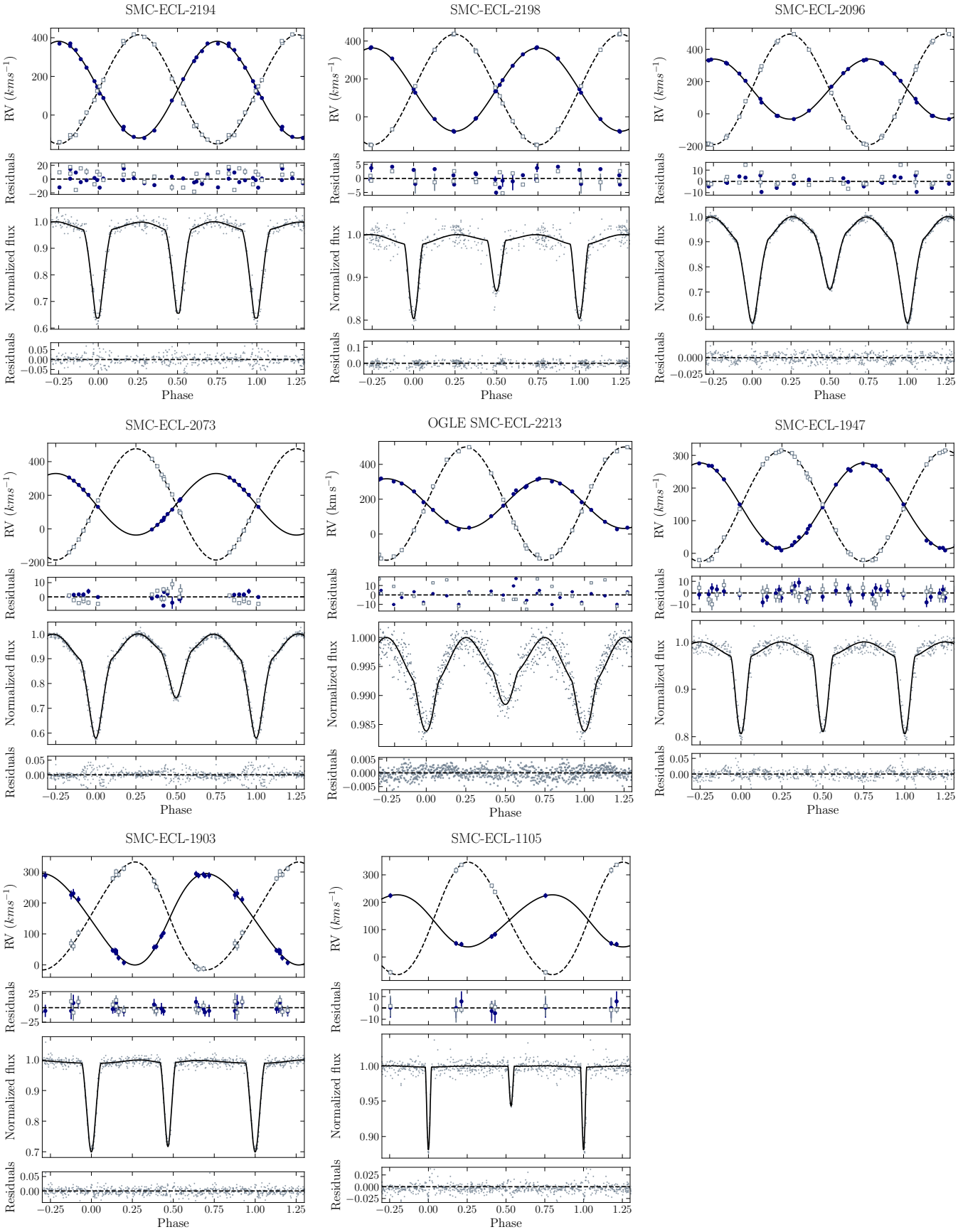

Figure 3. The figure presents a graphical representation of the spectroscopic orbit and light-curve models for the target systems. The first two panels illustrate the phase-folded spectroscopic orbit model. The continuous and dashed curves represent the more massive primary and the less massive secondary components, respectively. Filled circles represent observations for the primary component, whereas open squares indicate those for the secondary component, including their corresponding residuals.

Table 4
Physical Properties of the Systems

Parameter	SMC-ECL-2194		SMC-ECL-2198		SMC-ECL-2096		SMC-ECL-2073	
	Primary	Secondary	Primary	Secondary	Primary	Secondary	Primary	Secondary
Mode	Mode 2		Mode 2		Mode 5		Mode 5	
T_0	57001.0595(1)		57001.2875(2)		57000.7471(2)		57001.5821(1)	
P (day)	1.302942(2)		1.329851(3)		1.808929(2)		1.939408(2)	
$a \sin i$ ($R_\odot$)	12.932(107)		13.463(133)		18.903(117)		19.696(108)	
γ (km s^{-1})	160.4(9)		143.6(2)		152.7(4)		146.2(9)	
$K_{1,2}$ (km s^{-1})	241.7(1.2)	260.8(1.3)	220.1(1.4)	292.3(1.5)	186.3(1.5)	342.6(1.9)	183.1(6)	330.9(1.7)
e	0.022(1)		0.0		0.0		0.002(2)	
ω(deg)	257.4(1.1)		90		90		−37.1(1.8)	
q (M_2/M_1)	0.927(5)		0.753(6)		0.544(6)		0.553(9)	
i (deg)	75.9(7)		76.7(2)		78.8(7)		78.4(5)	
$T_{\rm eff\ 1,2}$ (K)	29 050[a][fix]	27 070(190)	26 300[a][fix]	20 340(130)	31 250[a][fix]	23 050(140)	30 000[a][fix]	21 050(160)
$\Omega_{1,2}$	4.8444(53)	4.5402(61)	2.6055(23)	3.3323(54)	2.4311(39)	2.6822(55)	2.3445(21)	2.2777
$A_{1,2}$	1.0[fix]		1.0[fix]		1.0[fix]		1.0[fix]	
$g_{1,2}$	1.0[fix]		1.0[fix]		1.0[fix]		1.0[fix]	
$X^c_{1,2}$	0.252	0.263	0.266	0.302	0.186	0.204	0.184	0.212
$l_1/(l_1+l_2)$	0.51(3)		0.91(4)		0.86(2)		0.88(5)	
$r_{1,2}$	0.2723(2)	0.2574(2)	0.4187 (1)	0.3153(2)	0.4732 (2)	0.4105 (1)	0.4653(4)	0.4815(4)
$\Sigma W(O-C)^2$	0.028		0.033		0.033		0.041	
Absolute parameters								
$M_{1,2}$ ($M_\odot$)	9.738(11)	9.025(13)	11.471(18)	8.636(10)	19.067 (11)	10.361(17)	18.753(23)	10.371(29)
$R_{1,2}$ ($R_\odot$)	3.631(19)	3.434(25)	5.791(3)	4.364(3)	9.125(6)	7.917(8)	9.365(4)	9.688(7)
$\log(g_{1,2})$ (cgs)	4.31(2)	4.32(3)	3.98(2)	4.11(2)	3.80(4)	3.66(5)	3.77(1)	3.48(1)
$(v_{1,2}\sin i)_{\rm calc}$ (km s^{-1})[d]	140(2)	133(4)	222(1)	169(1)	251(4)	223(7)	245(8)	249(11)
$\log(L_{1,2}/L_\odot)$	3.924(33)	3.752(34)	4.144(1)	3.797(2)	4.773(4)	4.196(6)	4.803(2)	4.204(3)
$M_{\rm bol\ 1,2}$ (mag)	−5.062(87)	−4.630(98)	−5.603(114)	−4.830(95)	−7.188(111)	−5.744(105)	−7.253(91)	−5.768(98)
$(m-M)_V$ (mag)	19.033(4)		19.014(11)		18.889(13)		19.214(35)	
$E(B-V)$ (mag)	0.188(87)		0.477(112)		0.546(15)		0.167(5)	
d (kpc)[b]	60.1(2.3)		62.3(2.1)		63.4(1.4)		66.3(1.8)	

Notes. Quantities in parentheses are uncertainties in the final digits of the preceding numbers. T_0 is given as BJD(TDB)–24 00000.0.
[a] $T_{\rm eff\ 1}$ were found in atmospheric analysis in Section 3.1.
[b] The JKTABSDIM distance is calculated from 2MASS magnitudes.

inside the SMC as well as their membership in the NGC 290 cluster.

3.4. Star Location within a Cluster versus Clustered Star Location

An unbiased evaluation enables us to examine the potential relationship between the NGC 290 cluster and the stars referred to in our study. Eight spectroscopically analyzed SMC eclipsing binaries are projected toward the open cluster NGC 290. In order to evaluate their possible physical association, we construct a consistent astrometric and structural reference framework for the cluster using Gaia DR3 data. The cluster is treated as a reference environment rather than as the primary scientific objective. Structural parameters, mean kinematics, and fundamental astrophysical properties are derived to assess the membership status of the eight targets through combined spatial, kinematic, and astrophysical consistency tests. The SMC targets lie within the projected field of NGC 290. To establish a reference cluster framework, we queried a circular region with 10′ of radius centered on (R.A., decl.) = (12.°801, −73.°1617) (A. P. Milone et al. 2023) from the Gaia DR3 archive, yielding 97,257 sources.

To reduce Milky Way (MW) foreground contamination, a parallax constraint of $\varpi \leqslant 0.2$ mas was applied (A. Strantzalis et al. 2024). At the SMC distance of approximately 60 kpc, this threshold efficiently removes most nearby foreground stars. In addition, we adopted the completeness-oriented threshold (Tcut = 0.31) defined by Ó. Jiménez-Arranz et al. (2023) to avoid excluding potential SMC members. This permissive threshold maximizes completeness at the expense of a higher level of MW contamination, which we account for in the subsequent structural and kinematic analysis. This reduced the sample to 12,162 high-probability SMC sources that remained within the 10′ region. This filtered sample provides the SMC-dominated stellar population within which NGC 290 is embedded.

To define the spatial extent of NGC 290 and provide a reference for membership testing, a radial density profile (RDP) was constructed and fitted with an I. King (1962) model using a minimum-χ^2 approach. The resulting structural parameters indicate a core radius of $r_c = 0.'280 \pm 0.'046$ and a limiting radius of $r_{\rm lim} = 5'$. The corresponding concentration parameter, $C = \log(r_{\rm lim}/r_c) = 1.4$, is consistent with previous determinations (M. Gatto et al. 2021) and indicates a moderately concentrated cluster with a compact core and a well-defined halo.

Cluster membership probabilities were computed in proper-motion space using the two-component mixture model of L. Balaguer-Núnez et al. (1998), which statistically separates

Table 5
Physical Properties of the Systems

Parameter	OGLE SMC-ECL-2213		OGLE SMC-ECL-1947		OGLE SMC-ECL-1903		OGLE SMC-ECL-1105	
	Primary	Secondary	Primary	Secondary	Primary	Secondary	Primary	Secondary
Mode	Mode 5		Mode 2		Mode 2		Mode 2	
T_0	57001.8070(2)		57002.5713(1)		57001.2523(2)		57009.5280(2)	
P (day)	2.323886(2)		2.401305(4)		3.942667(3)		9.057646(1)	
$a \sin i$ ($R_\odot$)	21.452(95)		14.343(203)		24.899(117)		53.655(469)	
γ (kms^{-1})	174.8(2)		153.4(3)		152.3(2)		139.1(8)	
$K_{1,2}$ (km s^{-1})	142.6(1.2)	324.7(1.3)	131.8(1.1)	170.5(1.3)	147.7(2.3)	174.5(2.8)	92.0(2.2)	207.9(2.4)
e	0.0		0.0		0.126(11)		0.076(7)	
ω(deg)	90		90		252.3(2.4)		58.4(3.1)	
q (M_2/M_1)	0.439(8)		0.773(5)		0.846(6)		0.463(9)	
i (deg)	80.4(1)		78.9(4)		84.4(2)		84.2(5)	
$T_{\rm eff\ 1,2}$ (K)	28 510[a][fix]	18 560(110)	12 280[a][fix]	11 990(140)	19 420[a][fix]	17 390(220)	32 300[a][fix]	22 820(150)
$\Omega_{1,2}$	2.7271(36)	2.7568	4.3289(41)	6.6640(44)	6.6976(23)	6.3021(54)	7.4728(39)	5.7796(52)
$A_{1,2}$	1.0[fix]		1.0[fix]		1.0[fix]		1.0[fix]	
$g_{1,2}$	1.0[fix]		1.0[fix]		1.0[fix]		1.0[fix]	
$X^c_{1,2}$	0.209	0.202	0.201	0.198	0.163	0.221	0.165	0.204
$l_1/(l_1+l_2)$	0.82(1)		0.82(5)		0.59(4)		0.75(3)	
$r_{1,2}$	0.4535(2)	0.3021(2)	0.2846(2)	0.1398(2)	0.1751(6)	0.1694(8)	0.1438(2)	0.1048(3)
$\Sigma W(O-C)^2$	0.035		0.031		0.033		0.096	
Absolute parameters								
$M_{1,2}$ ($M_\odot$)	17.803(70)	7.813(71)	4.103(39)	3.172(44)	7.370(98)	6.238(96)	17.556(77)	8.128(79)
$R_{1,2}$ ($R_\odot$)	9.866(42)	6.573(56)	4.160(55)	2.045(55)	4.389(95)	4.246(101)	7.755(52)	5.652(71)
$\log(g_{1,2})$ (cgs)	3.70(3)	3.71(5)	3.81(5)	4.32(5)	3.98(8)	4.02(2)	3.90(6)	3.89(7)
$(v_{1,2} \sin i)_{\rm calc}$ (km s^{-1})[d]	214(6)	143(7)	88(4)	43(3)	56(4)	54(7)	43(4)	31(8)
$\log(L_{1,2}/L_\odot)$	4.852(71)	3.715(52)	2.553(48)	1.863(64)	3.451(37)	3.145(65)	4.774(31)	3.937(66)
$M_{\rm bol\ 1,2}$ (mag)	−7.380(114)	−4.537(115)	−1.632(219)	0.091(310)	−3.878(92)	−3.113(163)	−7.185(76)	−5.091(163)
$(m-M)_V$ (mag)	19.999(318)		20.112(209)		19.104(133)		18.961(207)	
$E(B-V)$ (mag)	0.327(6)		0.011(109)		0.024(112)		0.419(37)	
d (kpc)[b]	64.7(3.2)		54.9(4.8)		58.5(6.1)		64.1(4.7)	

Notes. Quantities in parentheses are uncertainties in the final digits of the preceding numbers. T_0 is given as BJD(TDB)–24 00000.0.
[a] $T_{\rm eff\ 1}$ were found in atmospheric analysis in Section 3.1.
[b] The JKTABSDIM distance is calculated from 2MASS magnitudes.

cluster and field populations through a Gaussian description of their kinematic distributions. Parallaxes were used exclusively as a foreground filter and were not incorporated into the probability computation, because at the SMC distance the expected parallax (∼0.017 mas) is comparable to Gaia DR3 uncertainties and zero-point. Stars within $r_{\rm lim}$ were analyzed, and those with $P \geqslant 0.5$ were initially classified as probable members. Residual contamination in proper-motion space was further reduced by inspecting the color–magnitude diagram (CMD) morphology and theRDP behavior.

To derive robust mean kinematic properties, only stars within $r \leqslant 3r_c \approx 1'$ were considered, corresponding to the highest-density central region. From 74 probable members in this inner zone, the mean proper-motion components were determined as $(\mu_\alpha \cos\delta, \mu_\delta) = (0.609 \pm 0.169, -1.303 \pm 0.172)$ mas yr^{-1}, consistent with the SMC cluster kinematics reported by A. P. Milone et al. (2023). One inner-region member has a Gaia DR3 RV measurement ($V_r = 170.74 \pm 1.27$ km s^{-1}), adopted here as a representative cluster value.

Fundamental cluster parameters were derived by fitting the nonrotating PARSEC isochrones of A. Bressan et al. (2012) to the (G) versus ($BP - RP$) CMD constructed from stars within $r \leqslant 1'$. The best-fitting solution yields an age of 20 ± 5 Myr ($\log t = 7.3$), a distance of 63.4 ± 2.8 kpc corresponding to a distance modulus $\mu_G = 19.363 \pm 0.096$ mag, reddening values of $E(BP - RP) = 0.188 \pm 0.05$ mag and $E(B - V) = 0.133 \pm 0.035$ mag, and a metallicity of [Fe/H] = −0.7 dex. These values fall within the range of previous determinations (e.g., W. Narloch et al. 2021; A. P. Milone et al. 2023) and are adopted solely to provide a homogeneous reference for comparison with the target systems.

The eight SMC targets were evaluated for possible association with NGC 290 through combined spatial, kinematic, and astrophysical consistency tests. Seven of the stars lie within the adopted limiting radius of 5′, whereas OGLE SMC-ECL-1105 is located at a projected distance of 19′ from the cluster center. Although OGLE SMC-ECL-1105 exhibits proper-motion components consistent with the cluster mean within 1σ uncertainties, its large angular separation places it well beyond the region where the cluster density significantly exceeds the background level. Its spatial location, therefore, makes a bound association with NGC 290 unlikely.

For each star, the deviation of its proper motion from the cluster mean was quantified using an uncertainty-weighted metric. This analysis indicates that OGLE SMC-ECL-2194 is best interpreted as a field star, while OGLE SMC-ECL-2073 occupies a borderline position at the 2–3σ level. The remaining stars are consistent with cluster membership in proper-motion space. A secondary probability computation using the L. Balaguer-Núnez et al. (1998) formalism confirms that

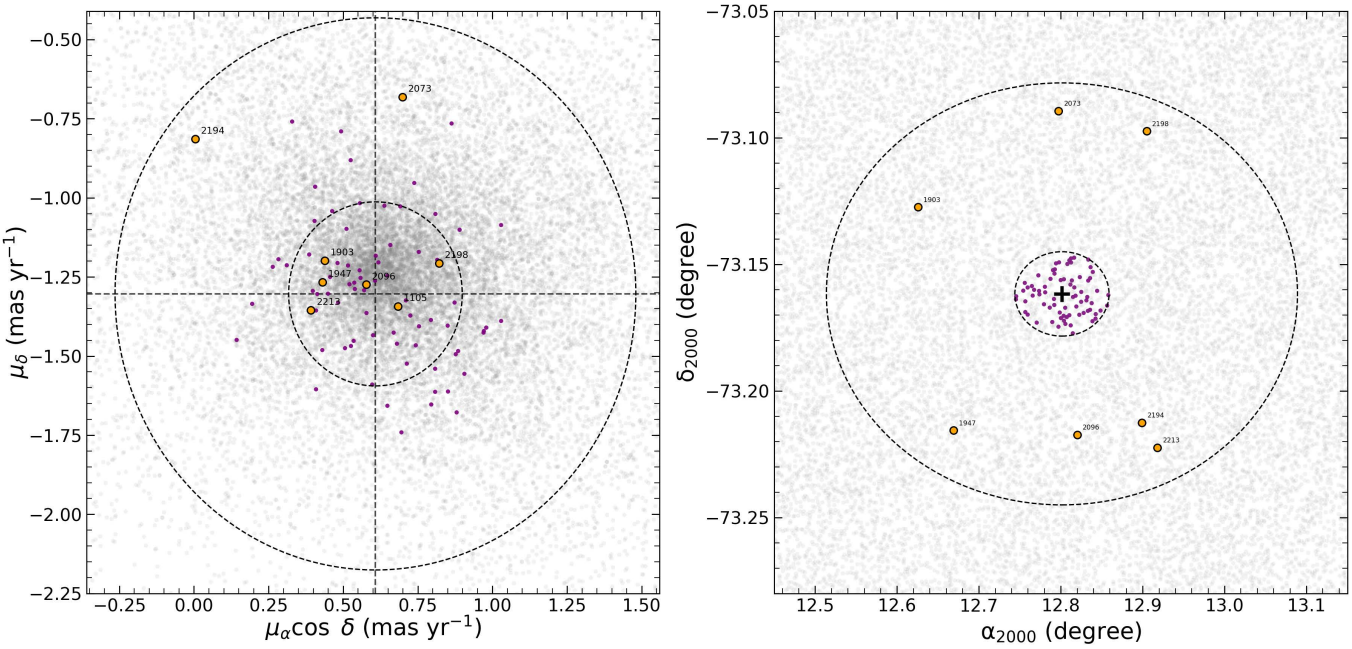

Figure 4. Left: vector point diagram of stars projected toward NGC 290. Small dots denote probable cluster members within the central region ($r \leqslant 1'$), shaded symbols represent field stars, and filled circles mark the eight SMC binaries. Dashed circles indicate the 1σ and 3σ boundaries of the cluster proper-motion distribution. Right: spatial distribution of stars within a $10'$ region. Dashed circles mark the inner region ($r \leqslant 1'$) and the limiting radius ($r_{\rm lim} = 5'$). SMC-1105, located at $19'$ from the center, lies outside the plotted spatial field.

OGLE SMC-ECL-2194 and OGLE SMC-ECL-2073 have probabilities close to zero, whereas the other six stars satisfy $P > 0.5$. Figure 4 illustrates the proper-motion distribution and the spatial configuration of the cluster members and the eight targets.

The final assessment incorporates stellar ages, distances, and radial velocities derived from the spectroscopic analysis. Figure 5 presents the CMD of NGC 290, including the probable cluster members, the best-fitting PARSEC isochrone, and the eight SMC targets. In this comparison, OGLE SMC-ECL-1903 appears as the most plausible candidate for association with NGC 290 based on its projected proximity and its location relative to the cluster sequence; however, the available constraints are insufficient for a secure membership assignment. The RV of OGLE SMC-ECL-2213 is consistent with the provisional cluster value, although its age appears younger than that of NGC 290. Within this framework, the cluster properties provide the environmental context for interpreting the physical nature of the eight spectroscopically analyzed SMC stars.

Building on the global spatial distribution discussed above, we note that sky-plane proximity alone does not provide a reliable basis for membership without a homogeneous structural and astrometric characterization of the cluster. The Gaia DR3–based framework established here enables a quantitative evaluation of membership likelihood. Using the derived constraints on distance, proper motion, and RV, we additionally examine the present-day dynamical state of each target within the Magellanic gravitational potential under two scenarios: an isolated SMC potential and a combined SMC +LMC configuration. This two-tiered approach places the concept of stellar "isolation" within a coherent environmental and dynamical context.

Kinematic analysis provides the primary basis for evaluating the likelihood of cluster association, while orbit integrations offer complementary context on the present-day dynamical state of the systems. Relying solely on static indicators, such as projected proximity and instantaneous proper-motion similarities, is insufficient to confirm a common origin. The phase-space structure in this region may be influenced by the irregular morphology of the SMC, uncertainties in distances and velocities, and the tidal influence of the Large Magellanic Cloud (LMC). Therefore, to model the mass distribution in the inner regions where star clusters predominantly form, we adopt the analytical `Hernquist` profile (L. Hernquist 1990). Orbital analyses were performed using the `galpy`[6] (J. Bovy 2015) library to integrate the orbits of the NGC 290 cluster and the eight SMC stars under a `Hernquist` potential in two scenarios: (1) the gravitational potential of the SMC alone and (2) the combined total potential of the SMC and LMC.

In these analyses, the orbits of the NGC 290 cluster and each of the eight investigated stars were modeled starting from their observed input parameters (α, δ, d, $\mu_\alpha \cos\delta$, μ_δ, V_r) to test for a shared dynamical origin. Although the `Hernquist` profile assumes spherical symmetry and thus cannot fully capture the tidally distorted morphology of the SMC (K. Bekki & S. Stanimirović 2009), it provides a first-order approximation to the enclosed distribution in the inner few kiloparsecs. Accordingly, in our simulations, we adopted a mass of $M_{\rm SMC} = 2.4 \times 10^9\ M_\odot$, corresponding to the mass enclosed within a galactocentric radius of $r \leqslant 3$ kpc, as derived from the H I rotation curve (S. Stanimirović et al. 2004), and a scale radius of $a_{\rm SMC} = 2.0$ kpc (K. Bekki & M. Chiba 2005; G. Besla et al. 2012). In the combined scenario, the gravitational potential of each galactic component was treated

[6] https://github.com/jobovy/galpy

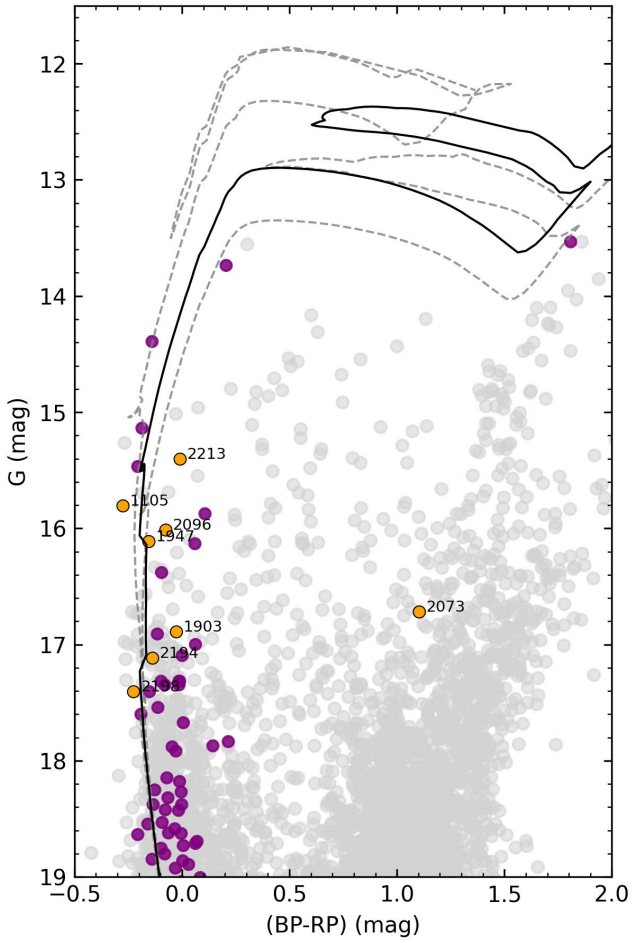

Figure 5. The CMD of NGC 290 for stars within $r \leqslant 1'$. Solid circle markers denote probable cluster members, and shaded markers represent other projected stars. The solid curve shows the best-fitting PARSEC isochrone corresponding to $\log t = 7.3$, $d = 63.4$ kpc, $E(B-V) = 0.13$ mag, and [Fe/H] $= -0.7$ dex. The eight SMC eclipsing binaries are shown as filled circles.

as an independent `Hernquist` sphere. For the LMC potential, we adopted a mass of $M_{\rm LMC} = 1.8 \times 10^{11}\ M_{\odot}$ and a scale radius of $a_{\rm LMC} = 20.0$ kpc, consistent with the total mass range constrained by stellar stream perturbations (D. Erkal et al. 2019; N. Shipp et al. 2021) and satellite kinematics (E. Vasiliev 2024). Within this SMC+LMC framework, the LMC was positioned as a static external potential at its present-day location; while a simplification, this approach provides a robust and sufficient basis for evaluating the instantaneous boundness of each target.

The orbital motions of star clusters and individual stars within a galactic potential provide critical insights into the dynamical structure and evolutionary history of the system. Diagnostic diagrams based on the conserved quantities of total orbital energy (E) and the vertical component of angular momentum (L_z), commonly referred to as Lindblad diagrams, provide a standard tool for kinematic classification (J. Binney & S. Tremaine 2008). In this normalization, the condition $E > 0$ corresponds to a formally unbound state. To evaluate the boundness of the targets, we first analyzed the kinematics under the isolated SMC potential (scenario 1). The resulting E versus L_z diagram (Figure 6) reveals a clear kinematic bifurcation.

As shown in Figure 6, the NGC 290 cluster and three SMC targets are gravitationally bound to the SMC ($E < 0$). Specifically, NGC 290 is deeply embedded within the potential well, locating at $E \approx -2500$ (km/s)^2 and $L_z \approx 10$ kpc km s^{-1}, which indicates a stable orbit consistent with the dynamical center of the SMC. Among the bound stars, SMC-ECL-2198 and SMC-ECL-2096 exhibit energy levels comparable to NGC 290, whereas SMC-ECL-1105 displays a retrograde or highly inclined orbit with negative angular momentum ($L_z \approx -20$ kpc km s^{-1}) while remaining bound. Conversely, the remaining systems occupy the unbound region ($E > 0$). Most notably, SMC-ECL-2194 emerges as an extreme outlier with $E \approx 29{,}000$ (km/s)^2 and $L_z \approx 100$ kpc km s^{-1}. SMC-ECL-2073 is also distinctly unbound ($E \approx 9000$ (km/s)^2), while the others cluster in the range of $E \approx 3000$–5000 (km/s)^2.

However, the interaction between the local SMC potential and the more massive neighboring LMC can radically alter the orbital energies of these systems (G. Besla et al. 2012). Evaluating the dynamical states under the combined SMC +LMC potential (scenario 2, Figure 6) demonstrates a significant downward vertical shift in the energy distribution.

The inclusion of the massive LMC deepens the total gravitational pool (K. Bekki & M. Chiba 2005), causing the majority of the stellar population that appeared unbound in the isolated SMC model to drop into the $E < 0$ regime. For instance, the energy of SMC-ECL-2073 decreases drastically from +9000 to approximately −7000 (km/s)^2, illustrating that even if an object escapes the immediate vicinity of the SMC, it remains trapped by the LMC's deep gravitational well. Similarly, the natively bound NGC 290 cluster becomes even more tightly bound to the system, shifting to $E \approx -20{,}000$ (km/s)^2.

Despite this systematic energy reduction, the extreme outlier SMC-ECL-2194 remains formally unbound, with its energy decreasing only to $E \approx 11{,}000$ (km/s)^2. This behavior is consistent with a high-velocity runaway ejected via a supernova in a binary system (the "binary supernova scenario"; A. Blaauw 1961) or through dynamical interactions in dense stellar environments (A. Poveda et al. 1967). Alternatively, it may represent a high-velocity interloper traversing the region, potentially linked to three-body interactions involving a massive black hole or dense cluster cores (J. G. Hills 1988; W. R. Brown 2015). Overall, this comparison highlights that kinematic interpretation in this region should not rely solely on an isolated SMC potential. Systems that appear to be escaping the SMC may remain bound to the broader Magellanic gravitational environment and could trace large-scale structures such as the Magellanic Bridge (L. T. Gardiner & M. Noguchi 1996; G. Besla et al. 2007).

In the following section, we examine whether the ages inferred from the binary solutions are consistent with the cluster reference framework and use this comparison to refine the interpretation of cluster association versus field origin.

4. Evolutionary Status

A comparison of the components of each system with the theoretical evolution tracks in the Kiel diagram ($\log T_{\rm eff} - \log(g)$ diagram) can be made by merging the results of the spectroscopic and photometric analyses. This process leads to an estimation of the evolutionary status of each component. The main benefit of the Kiel diagram is the ability

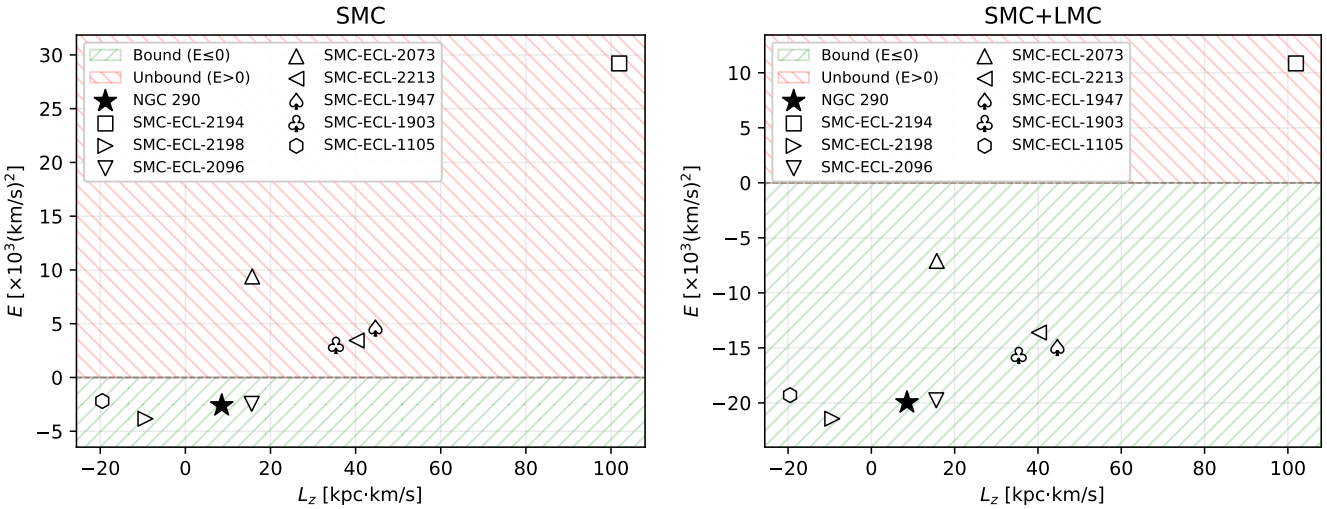

Figure 6. The Lindblad diagrams under the SMC potential (left) and the combined SMC+LMC potentials (right). The dashed areas represent the bound and unbound regions (see text for more information).

to simplify the comparison of stars with predictions of stellar evolution, all without requiring any prior knowledge of their distance. An exemplary application of this technique can be found in R. P. Kudritzki (1976). The relatively large uncertainties of spectroscopic gravity determinations often negatively impact the comparison with stellar evolution calculations. Thus, the $\log g$ value of each star in the Kiel diagram has been determined by the results of its combined light and velocity curve analysis, rather than by atmospheric parameters, due to conflicting factors. By combining the stellar abundances estimated from the atmospheric analyses, we successfully estimated the stellar ages from the evolutionary tracks.

To show the evolutionary status of our samples, we use the MESA Isochrones and Stellar Tracks (MIST[7] v1.2, A. Dotter 2016; J. Choi et al. 2016), which is generated by the Modules for Experiments in Stellar Astrophysics (MESA[8]) package (B. Paxton et al. 2011, 2013, 2015) and serves as a thorough and updated version of the stellar evolution model for a wide range of metallicities. The evolutionary tracks shown in Figure 7 were generated using the MIST web interpolator, which made the task easier. Then we compared our results with these evolutionary tracks.

The Kiel diagrams of SMC-ECL-2194 and SMC-ECL-2198 represent a complex case. The light and RV curves of SMC-ECL-2194 provide reliable results with small errors; however, they do not fully match the predicted evolutionary paths of the system's components. However, when plotted on the Kiel diagram, utilizing temperature and $\log(g)$ values derived from atmospheric analysis, SMC-ECL-2194 demonstrates increased consistency. The circumstances surrounding SMC-ECL-2198 are totally separate. The atmospheric analysis of SMC-ECL-2198 reveals values that, when plotted on the H-R diagram, demonstrate that the system's components adhere to their expected evolutionary path. Nevertheless, its position on the H-R diagram, as indicated by the light-curve analysis results, contradicts established evolutionary trends. The discrepancies in the evolutionary paths of both systems, SMC-ECL-2194 and SMC-ECL-2198, are proposed to arise from the light curves, which exhibit limited sensitivity and a restricted number of data points. As visible in Figure 3, the significant scattering of the light curve of the star SMC-ECL-2198 significantly affects the reliability of the analysis results, which may be attributed to incorrect modeling. We would like to highlight that the results of the solution cannot be considered reliable with respect to the absolute parameters of the secondary star. However, the atmospheric analyses utilizing GIRAFFE data, despite their low spectral resolution, are generally reliable for all stars. Observations of additional stars provide evidence for this hypothesis. The considerable scattering and restricted data in the light curves of these two systems may inherently explain the discrepancies with the evolutionary pathways.

A comparison of the astrophysical parameters of the SMC-ECL-2096 and SMC-ECL-2073 systems, derived from spectroscopic and combined photometric+RV analyses, shows minor discrepancies as well as notable similarities. The analysis of these binary systems represents significant advances compared to earlier research. The companion stars in both systems have filled their Roche lobes, and the two secondaries are located significantly away from the zero-age main sequence. The systems show notable similarities regarding essential astrophysical characteristics. This feature allows for the identification of different stellar parameters that may assist in clarifying the evolutionary status of the systems. This sophisticated system is especially intriguing, as it provides observational constraints for theoretical binary evolutionary models. Similar analyses have been performed for B-type stars (K. Pavlovski et al. 2009), but investigations involving systems made up of two evolved early-type stars are quite uncommon (e.g., Plaskett's star as mentioned by N. Linder et al. 2008). Analysis of these two systems emphasizes the need to develop theoretical binary evolutionary models.

Overall, the majority of the analyzed systems are unlikely to be members of a bound stellar cluster in the SMC. Nevertheless, one or two cases remain plausible within the current astrometric and evolutionary uncertainties and therefore cannot be excluded on firm grounds.

The systems referred to as field stars can be formed of isolated stars, recognized for their existence, as there are isolated massive stars that do not have any nearby massive companions associated

[7] https://mist.science/
[8] https://mesastar.org/

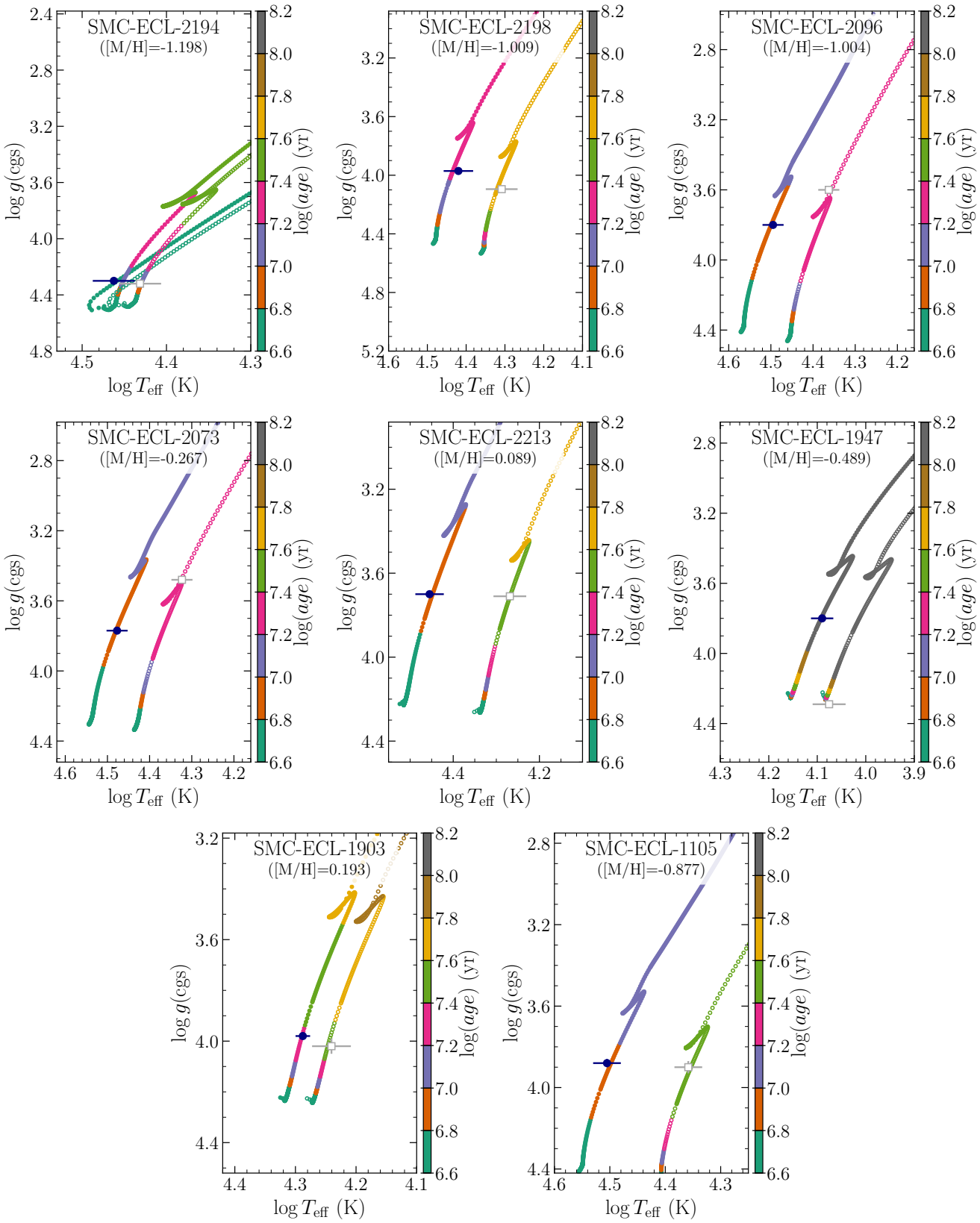

Figure 7. Our findings are compared with the MESA evolution tracks on Kiel diagrams within the $\log T_{\rm eff}$ / $\log(g)$ planes. The primary component is shown by filled circles, whereas the secondary components are shown as open squares, each with error bars as outlined in Tables 4 and 5. The colored points represent the evolutionary tracks linked to the calculated component masses, with the colors denoting stellar age, as indicated by the color bars on the right side of the plots.

with them. Studies examining observations (P. Massey 2002) and statistical analyses (C. Weidner & P. Kroupa 2004) indicate that the initial mass function of field stars differs from that focused in stellar clusters. Additionally, theories propose that various physical factors may influence the formation of different massive stars in the field (e.g., Y. Li et al. 2003). The fundamental

question for theories regarding massive star formation is whether OB stars are capable of forming in isolation. The inquiry into star formation, specifically regarding the potential for massive stars to evolve in isolation versus within stellar clusters, holds significant relevance for the understanding of massive star formation theories and the stellar initial mass function within entire galaxies. Although this question seems straightforward, providing an answer is quite complex. The study of these eight stars serves as an exemplary case of isolated Galactic massive star formation, primarily due to the presence of nearby indicators of recent star formation in the SMC, so that the more precise estimate of the absolute parameters is crucial.

5. Summary and Discussion

The stellar population of the observable SMC, which represents its history of interaction with the LMC, is what defines it. The connection between their distances, metallicities, and ages helps to explain these effects. We selected eight stars that we believe exemplify this representation and have not been previously studied. We derived the fundamental physical quantities, such as masses and radii, for all our systems with moderate precision and looked for isolated stars in a galaxy outside of the MW's immediate vicinity.

All eight stars are classified as massive stars and share similarities in terms of temperature, radius, and mass, with the exception of SMC-ECL-1947 and SMC-ECL-1903. While all analyses of the two systems were carried out efficiently and their astrophysical parameters were obtained with relatively small errors, there is a lack of agreement with the theoretical evolutionary paths. The systems SMC-ECL-2194 and SMC-ECL-2198 symbolize the primary challenge for obtaining an easy understanding of the discrepancies between the observed and predicted positions of the objects in the H-R diagram. The observed spectra's low SNR restricts the precision of the derived surface temperatures and metallicities from spectroscopy. We achieved temperature uncertainties of less than 300 K for six stars, while the other two stars showed uncertainties of approximately 700 K. This section of the analysis suggests that there are likely still opportunities to enhance these measurements through further spectroscopic observations.

The PLATO satellite presents a substantial opportunity to deepen our understanding of these sources. Upon becoming operational, the PLATO telescope's field of view will include approximately 50% of the SMC (J. Southworth et al. 2026, in preparation). We believe that this will provide an opportunity to enhance our models and validate the concept that the targets are intrinsically variable.

A further important aspect of this study concerns the environmental context of the eight systems. Although the targets are projected toward the open cluster NGC 290, a homogeneous Gaia DR3-based structural and kinematic analysis demonstrates that firm cluster membership can only be established in a limited number of cases. Seven systems lie within the adopted limiting radius of the cluster, yet proper-motion and spatial diagnostics indicate that at least two objects (SMC-ECL-2194 and SMC-ECL-2073) are more consistent with a field classification. OGLE SMC-ECL-1903 emerges as the most plausible candidate for association with NGC 290; however, the available astrometric and evolutionary constraints remain insufficient for a definitive membership assessment. We note that probabilistic membership assignments based on proper-motion consistency do not automatically guarantee long-term dynamical association.

The orbital analysis further shows that several systems that appear formally unbound in an isolated SMC potential become bound when the gravitational influence of the LMC is included. This highlights the importance of adopting a global Magellanic framework when interpreting stellar kinematics in this region. In particular, SMC-ECL-2194 remains dynamically distinct even in the combined SMC+LMC configuration, suggesting a possible high-velocity or runaway nature. Overall, our results indicate that the majority of the systems are not securely associated with NGC 290 but are instead embedded within the broader dynamical structure of the Magellanic system.

These findings imply that apparent isolation in projection does not necessarily correspond to dynamical isolation. The combination of precise astrometry and orbit integration demonstrates that the concept of "isolated massive stars" in the SMC must be evaluated within the full Magellanic gravitational context rather than solely through sky-plane proximity.

Acknowledgments

We thank the anonymous reviewer for their careful reading of our manuscript and their many insightful comments and suggestions. The following internet-based resources were used in the research for this paper: the NASA Astrophysics Data System and the SIMBAD database operated at CDS, as well as the open-source Python packages ASTROPY http://www.astropy.org (Astropy Collaboration et al. 2013), MATPLOTLIB (J. D. Hunter 2007), NUMPY (C. R. Harris et al. 2020), and PANDAS (J. Reback et al. 2020). This work is based on data from the Kepler mission. Kepler was competitively selected as the tenth Discovery mission. Funding for this mission is provided by NASA's Science Mission Directorate. The photometric data were obtained from the Mikulski Archive for Space Telescopes (MAST). This work has also made use of data from the European Space Agency (ESA) mission Gaia (http://www.cosmos.esa.int/gaia), processed by the Gaia Data Processing and Analysis Consortium (DPAC, http://www.cosmos.esa.int/web/gaia/dpac/consortium).
This research has also made use of the "Aladin sky atlas" developed at CDS, Strasbourg Observatory, France. The spectra used in this study were obtained by using the available spectra that were collected by the program IDs; 60.A-9022(C), 0104.A-9001(A), 0106.A-9006(A), 073.C-0337(A), and 178.D-0361(F). This article is a part of the PhD thesis of M.K.

Appendix

Table A1 presents the velocity values for both components of our SB2 systems, including their associated errors and the heliocentric Julian dates of the observations.

Table A1
Measured RVs of the Components in Each Target System, along with Statistical Uncertainties (σ_{RV})

HJD (24,00000+)	RV_1 (km s^{-1})	σ_{RV_1} (km s^{-1})	RV_2 (km s^{-1})	σ_{RV_2} (km s^{-1})	Instrument
SMC-ECL-2194					
52959.54228	−47.7	6.3	378.7	7.3	GIRAFFE
52959.71149	−78.0	3.1	417.6	8.3	GIRAFFE
52960.53937	259.9	5.1	51.4	3.6	GIRAFFE
52960.67779	111.7	2.3	216.9	3.5	GIRAFFE
52961.53366	386.2	3.7	−86.1	0.1	GIRAFFE
52961.70896	361.2	5.7	−61.0	2.3	GIRAFFE
52962.54352	113.7	3.7	214.1	4.3	GIRAFFE
52962.72694	323.4	5.6	−4.7	3.5	GIRAFFE
52963.53348	−78.7	1.4	417.2	3.9	GIRAFFE
52964.53579	170.1	2.4	153.2	2.9	GIRAFFE
52964.55598	148.2	1.4	175.2	1.9	GIRAFFE
52964.75008	−36.7	4.1	376.2	1.9	GIRAFFE
52965.52868	399.5	0.2	−95.7	1.9	GIRAFFE
52965.70366	309.2	3.3	2.7	1.9	GIRAFFE
52966.54541	222.7	3.5	92.2	1.9	GIRAFFE
52966.70023	366.6	4.2	−63.7	1.9	GIRAFFE
56567.64033	−37.0	2.2	370.2	1.9	GIRAFFE
56569.60045	336.5	2.5	−29.7	1.9	GIRAFFE
56587.53031	333.2	1.6	−25.7	1.9	GIRAFFE
56599.72156	190.2	1.7	124.7	1.9	GIRAFFE
56621.67172	365.0	1.7	−67.7	1.9	GIRAFFE
SMC-ECL-2198					
52959.54229	364.1	1.3	−146.8	5.3	GIRAFFE
52959.71150	289.1	1.3	-45.1	5.3	GIRAFFE
52960.53938	162.3	1.3	124.1	5.3	GIRAFFE
52960.67780	288.1	1.3	-51.1	5.3	GIRAFFE
52961.53366	−75.1	1.3	433.1	5.3	GIRAFFE
52961.70897	1.1	1.3	339.1	5.3	GIRAFFE
52962.54352	122.1	1.3	180.1	5.3	GIRAFFE
52963.53348	365.1	1.3	−146.8	5.3	GIRAFFE
52964.53580	168.5	1.3	117.1	5.3	GIRAFFE
52964.55599	185.1	1.3	88.1	5.3	GIRAFFE
52964.75009	340.1	1.3	−118.8	5.3	GIRAFFE
52965.52869	−75.5	1.3	435.1	5.3	GIRAFFE
52965.70367	14.1	1.3	324.1	5.3	GIRAFFE
52966.54542	98.1	1.3	202.1	5.3	GIRAFFE
52966.70024	−29.1	1.3	372.1	5.3	GIRAFFE
56621.67173	205.1	1.3	69.3	5.3	GIRAFFE
SMC-ECL-2096					
52959.52870	204.6	0.5	78.1	0.8	GIRAFFE
52959.70298	92.7	3.4	272.1	4.9	GIRAFFE
52960.53008	168.2	0.8	129.9	1.7	GIRAFFE
52960.66981	252.3	1.1	-27.3	1.1	GIRAFFE
52961.52452	70.2	1.5	294.9	1.7	GIRAFFE
52961.70180	−12.5	1.1	442.9	1.6	GIRAFFE
52962.53471	277.5	1.0	-84.3	0.7	GIRAFFE
52962.71513	332.3	0.6	−185.2	0.9	GIRAFFE
52963.52455	−13.0	0.9	452.2	1.7	GIRAFFE
52964.52610	331.1	1.0	−185.3	0.9	GIRAFFE
52964.55559	336.3	0.6	−191.4	1.1	GIRAFFE
52964.74101	311.1	0.5	−137.1	0.4	GIRAFFE
52965.51943	−32.9	1.0	494.4	2.5	GIRAFFE
52965.69577	19.6	0.4	397.3	0.5	GIRAFFE
52966.53717	316.1	0.7	−147.6	1.4	GIRAFFE
52966.69306	249.4	0.7	-18.2	1.0	GIRAFFE
SMC-ECL-2073					
52959.52871	305.4	0.6	−139.3	0.7	GIRAFFE
52959.70299	232.5	1.6	-9.8	1.7	GIRAFFE
52960.53009	-3.3	0.6	416.1	1.2	GIRAFFE
52960.66982	53.3	1.2	308.2	1.5	GIRAFFE
52961.52453	286.8	0.6	−107.6	0.8	GIRAFFE
52961.70181	202.2	1.8	48.0	1.6	GIRAFFE
52962.53472	23.8	0.8	372.3	1.3	GIRAFFE
52962.71514	114.7	4.3	204.6	3.8	GIRAFFE
52963.52456	261.1	0.9	-62.7	1.1	GIRAFFE
52964.52611	47.4	2.0	322.5	2.3	GIRAFFE
52964.55560	66.6	1.5	295.1	2.1	GIRAFFE
52964.74102	168.3	0.3	103.1	0.6	GIRAFFE
52965.51943	233.2	1.0	-9.8	1.3	GIRAFFE
52965.69578	130.7	0.7	169.1	1.3	GIRAFFE
52966.53718	88.3	2.0	258.6	3.2	GIRAFFE
52966.69307	176.3	3.2	94.4	4.3	GIRAFFE
SMC-ECL-2213					
52959.52870	229.6	0.2	66.6	0.2	GIRAFFE
52959.70298	268.6	0.2	-65.3	0.2	GIRAFFE
52960.53008	182.6	0.2	129.6	0.2	GIRAFFE
52960.66981	138.4	0.2	273.4	0.2	GIRAFFE
52961.52452	102.6	0.2	348.6	0.2	GIRAFFE
52961.70181	162.6	0.2	196.6	0.2	GIRAFFE
52962.53471	289.8	0.2	-92.3	0.2	GIRAFFE
52962.71513	244.6	0.2	21.6	0.2	GIRAFFE
52963.52455	36.6	0.2	498.6	0.2	GIRAFFE
52964.52610	312.6	0.2	−118.3	0.2	GIRAFFE
52964.55559	318.6	0.2	−140.3	0.2	GIRAFFE
52964.74101	301.6	0.2	−128.3	0.2	GIRAFFE
52965.51943	70.1	0.2	426.6	0.2	GIRAFFE
52965.69577	27.7	0.2	474.6	0.2	GIRAFFE
52966.53717	250.6	0.2	36.6	0.2	GIRAFFE
52966.69306	275.6	0.2	-83.3	0.2	GIRAFFE
SMC-ECL-1947					
52959.52870	34.7	4.1	295.7	5.1	GIRAFFE
52959.70297	62.7	4.1	244.7	5.1	GIRAFFE
52960.53008	275.4	4.1	−20.5	5.1	GIRAFFE
52960.66981	268.5	4.1	−21.2	5.1	GIRAFFE
52961.52452	30.6	4.1	290.6	5.1	GIRAFFE
52961.70180	16.7	4.1	310.7	5.1	GIRAFFE
52962.53471	210.4	4.1	70.7	5.1	GIRAFFE
52962.71513	258.0	4.1	3.0	5.1	GIRAFFE
52963.52455	149.8	4.1	135.8	5.1	GIRAFFE
52964.52610	74.8	4.1	232.3	5.1	GIRAFFE
52964.55558	84.6	4.1	226.6	5.1	GIRAFFE
52964.74101	140.6	4.1	149.6	5.1	GIRAFFE
52965.51942	267.6	4.1	−17.3	5.1	GIRAFFE
52965.69577	226.5	4.1	48.6	5.1	GIRAFFE
52966.53717	9.0	4.1	315.0	5.1	GIRAFFE
52966.69306	25.0	4.1	307.0	5.1	GIRAFFE
56567.63244	253.2	4.1	8.0	5.1	GIRAFFE
56569.59335	253.0	4.1	-2.9	5.1	GIRAFFE
56587.51531	39.1	4.1	272.4	5.1	GIRAFFE
56599.71409	16.4	4.1	307.4	5.1	GIRAFFE
56621.66566	49.4	4.1	276.4	5.1	GIRAFFE
SMC-ECL-1903					
52959.52871	225.9	14.4	69.5	14.4	GIRAFFE
52959.70298	211.2	10.5	103.4	10.5	GIRAFFE
52960.53009	46.6	7.8	279.1	7.8	GIRAFFE
52960.66981	22.6	8.7	291.3	8.7	GIRAFFE
52961.52452	55.9	9.7	271.2	9.7	GIRAFFE
52961.70181	93.2	9.8	⋯	⋯	GIRAFFE

Table A1
(Continued)

HJD (24,00000+)	RV_1 (km s^{-1})	σ_{RV_1} (km s^{-1})	RV_2 (km s^{-1})	σ_{RV_2} (km s^{-1})	Instrument
52962.53471	294.3	9.0	-6.3	9.0	GIRAFFE
52962.71513	292.1	8.6	−12.2	8.6	GIRAFFE
52963.52456	230.9	14.3	60.2	14.3	GIRAFFE
52964.52610	43.5	11.8	⋯	⋯	GIRAFFE
52964.55559	38.2	8.1	291.5	8.1	GIRAFFE
52964.74101	7.1	8.6	311.1	8.6	GIRAFFE
52965.51943	59.3	8.9	252.2	8.9	GIRAFFE
52965.69578	102.9	7.4	⋯	⋯	GIRAFFE
52966.53718	288.5	8.7	−13.5	8.7	GIRAFFE
52966.69306	287.2	7.4	⋯	⋯	GIRAFFE
56599.71409	45.3	8.5	301.5	8.5	GIRAFFE
56621.66566	288.7	10.6	⋯	⋯	GIRAFFE
SMC-ECL-1105					
56567.63245	46.3	8.9	336.7	3.1	GIRAFFE
56569.59336	82.8	8.9	237.7	6.3	GIRAFFE
56587.51531	74.7	8.9	260.7	4.2	GIRAFFE
56599.71408	224.2	8.9	−56.2	9.2	GIRAFFE
56621.66564	49.6	8.9	316.7	11.1	GIRAFFE

(This table is available in machine-readable form in the online article.)

ORCID iDs

Ö. Çakirli https://orcid.org/0000-0002-8814-8303
B. Hoyman https://orcid.org/0000-0001-8332-522X
O. Özdarcan https://orcid.org/0000-0003-4820-3950
T. Yontan https://orcid.org/0000-0002-5657-6194
R. Canbay https://orcid.org/0000-0003-2575-9892

References

Adibekyan, V., Delgado-Mena, E., Figueira, P., et al. 2016, A&A, 592, A87
Astropy Collaboration, Robitaille, T. P., Tollerud, E. J., et al. 2013, A&A, 558, A33
Balaguer-Núnez, L., Tian, K. P., & Zhao, J. L. 1998, A&AS, 133, 387
Bekki, K., & Chiba, M. 2005, MNRAS, 356, 680
Bekki, K., & Stanimirović, S. 2009, MNRAS, 395, 342
Besla, G., Kallivayalil, N., Hernquist, L., et al. 2007, ApJ, 668, 949
Besla, G., Kallivayalil, N., Hernquist, L., et al. 2012, MNRAS, 421, 2109
Binney, J., & Tremaine, S. 2008, Galactic Dynamics: Second Edition (Princeton Univ. Press)
Blaauw, A. 1961, BAN, 15, 265
Blanco-Cuaresma, S. 2019, MNRAS, 486, 2075
Blanco-Cuaresma, S., Soubiran, C., Heiter, U., & Jofré, P. 2014, A&A, 569, A111
Bovy, J. 2015, ApJS, 216, 29
Bressan, A., Marigo, P., Girardi, L., et al. 2012, MNRAS, 427, 127
Brown, W. R. 2015, ARA&A, 53, 15
Çakırlı, Ö., Hoyman, B., & Özdarcan, O. 2023, MNRAS, 523, 1676
Chiosi, E., & Vallenari, A. 2007, A&A, 466, 165
Choi, J., Dotter, A., Conroy, C., et al. 2016, ApJ, 823, 102
di Benedetto, G. P. 1998, A&A, 339, 858
Dotter, A. 2016, ApJS, 222, 8
Doyle, A. P., Davies, G. R., Smalley, B., Chaplin, W. J., & Elsworth, Y. 2014, MNRAS, 444, 3592
Elmegreen, B. G. 2011, EAS, 51, 45
Erkal, D., Belokurov, V., Laporte, C. F. P., et al. 2019, MNRAS, 487, 2685
Foreman-Mackey, D., Hogg, D. W., Lang, D., & Goodman, J. 2013, PASP, 125, 306
Gardiner, L. T., & Noguchi, M. 1996, MNRAS, 278, 191
Gatto, M., Ripepi, V., Bellazzini, M., et al. 2021, MNRAS, 507, 3312
Girardi, L., Bertelli, G., Bressan, A., et al. 2002, A&A, 391, 195
Górski, M., Zgirski, B., Pietrzyński, G., et al. 2020, ApJ, 889, 179
Gouliermis, D. A., Bestenlehner, J. M., Brandner, W., & Henning, T. 2010, A&A, 515, A56
Graczyk, D., Pietrzyński, G., Thompson, I. B., et al. 2020, ApJ, 904, 13
Güzel, O., & Özdarcan, O. 2020, CoSka, 50, 535
Harris, C. R., Millman, K. J., van der Walt, S. J., et al. 2020, Natur, 585, 357
Haschke, R., Grebel, E. K., & Duffau, S. 2011, AJ, 141, 158
Hénault-Brunet, V., Evans, C. J., Sana, H., et al. 2012, A&A, 546, A73
Hernquist, L. 1990, ApJ, 356, 359
Hilditch, R. W., Howarth, I. D., & Harries, T. J. 2005, MNRAS, 357, 304
Hills, J. G. 1988, Natur, 331, 687
Hony, S., Gouliermis, D. A., Galliano, F., et al. 2015, MNRAS, 448, 1847
Houdashelt, M. L., Bell, R. A., Sweigart, A. V., & Wing, R. F. 2000, AJ, 119, 1424
Hunter, J. D. 2007, CSE, 9, 90
Hutchings, J. B., & Thompson, I. B. 1988, ApJ, 331, 294
Jiménez-Arranz, Ó., Romero-Gómez, M., Luri, X., & Masana, E. 2023, A&A, 672, A65
King, I. 1962, AJ, 67, 471
Kudritzki, R. P. 1976, A&A, 52, 11
Lada, C. J., & Lada, E. A. 2003, ARA&A, 41, 57
Lamb, J. B., Oey, M. S., Segura-Cox, D. M., et al. 2016, ApJ, 817, 113
Li, Y., Klessen, R. S., & Mac Low, M.-M. 2003, ApJ, 592, 975
Linder, N., Rauw, G., Martins, F., et al. 2008, A&A, 489, 713
Massey, P. 2002, ApJS, 141, 81
Milone, A. P., Cordoni, G., Marino, A. F., et al. 2023, A&A, 672, A161
Narloch, W., Pietrzyński, G., Gieren, W., et al. 2021, A&A, 647, A135
Oey, M. S., & Lamb, J. B. 2012, ASPC, 465, 431
Pavlovski, K., Tamajo, E., Koubský, P., et al. 2009, MNRAS, 400, 791
Pawlak, M., Soszyński, I., Udalski, A., et al. 2016, AcA, 66, 421
Paxton, B., Bildsten, L., Dotter, A., et al. 2011, ApJS, 192, 3
Paxton, B., Cantiello, M., Arras, P., et al. 2013, ApJS, 208, 4
Paxton, B., Marchant, P., Schwab, J., et al. 2015, ApJS, 220, 15
Pilecki, B., Gieren, W., Smolec, R., et al. 2017, ApJ, 842, 110
Portegies Zwart, S. F., McMillan, S. L. W., & Gieles, M. 2010, ARA&A, 48, 431
Poveda, A., Ruiz, J., & Allen, C. 1967, BOTT, 4, 86
Rafert, J. B., & Twigg, L. W. 1980, MNRAS, 193, 79
Ramírez, I., & Meléndez, J. 2005, ApJ, 626, 465
Reback, J., McKinney, W., McKinney, W., et al. 2020, pandas-dev/pandas: Pandas, v1.0.0, Zenodo, doi:10.5281/zenodo.3630805
Ricker, G. R., Winn, J. N., Vanderspek, R., et al. 2015, JATIS, 1, 014003
Roberts, M. S. 1957, PASP, 69, 59
Sana, H. 2013, in Massive Stars: From alpha to Omega, 26
Sana, H., de Mink, S. E., de Koter, A., et al. 2012, Sci, 337, 444
Sana, H., de Koter, A., de Mink, S. E., et al. 2013, A&A, 550, A107
Shipp, N., Erkal, D., Drlica-Wagner, A., et al. 2021, ApJ, 923, 149
Skowron, D. M., Skowron, J., Udalski, A., et al. 2021, ApJS, 252, 23
Sousa, S. G., Santos, N. C., Adibekyan, V., Delgado-Mena, E., & Israelian, G. 2015, A&A, 577, A67
Southworth, J., Maxted, P. F. L., & Smalley, B. 2005, A&A, 429, 645
Stanimirović, S., Staveley-Smith, L., & Jones, P. A. 2004, ApJ, 604, 176
Strantzalis, A., Lazarou, D., Hatzidimitriou, D., et al. 2024, A&A, 681, A24
Tonry, J., & Davis, M. 1979, AJ, 84, 1511
Udalski, A. 2003, AcA, 53, 291
Udalski, A., Kubiak, M., & Szymanski, M. 1997, AcA, 47, 319
Udalski, A., Szymański, M. K., & Szymański, G. 2015, AcA, 65, 1
van Hamme, W. 1993, AJ, 106, 2096
Vasiliev, E. 2024, MNRAS, 527, 437
Watson, C. L., Henden, A. A., & Price, A. 2006, SASS, 25, 47
Weidner, C., & Kroupa, P. 2004, MNRAS, 348, 187
Wilson, R. E. 1979, ApJ, 234, 1054
Wilson, R. E., & Devinney, E. J. 1971, ApJ, 166, 605
Wilson, R. E., & Van Hamme, W. 2014, ApJ, 780, 151